6

Effect of Decoration of Carbon Nanofibers on ZnO Nanostructures for Hydrogen Detection

In this chapter, the impact of carbon nanofibers loading on ZnO nanostructures for improvement in sensing response towards hydrogen gas has been investigated. PAN/(PAN-b-PMMA) derived electrospun nanoporous carbon nanofibers are chosen as decoration nanomaterials due to their high surface area with porous structures, which further improve the sensing performance on combination with ZnO nanostructures. Different concentrations of carbon nanofibers are used to study the structural, morphological, and electrical and gas sensing behaviour of pure carbon nanofibers and carbon nanofibers loaded ZnO nanostructures. Improvement in sensing response is correlated to the formation of p-n heterojunction because of p-type and n-type properties of carbon nanofibers and ZnO, respectively. A possible gas sensing mechanism is discussed in the end of this chapter.

6.1 INTRODUCTION

Recently, the use of carbonaceous materials like carbon nanotubes, graphene, and activated carbons have gained much attention for enhancing the sensing response towards hydrogen gas at mild operating temperature [Bhati *et al.,* 2018; Kumar *et al.,* 2006; Singh *et al.,* 2017]. Carbon nanofibers (CNF) have demonstrated superior gas sensor properties due to their large surface area, good conductivity, and availability of nanoporous structures consisting of hydrophobic graphene sheets and hydrophilic functionalized groups on its surface [Seredych *et al.,* 2008]. As a consequence, small-sized gas molecules like, hydrogen may easily diffuse inside the nanoporous structures of CNF, and interact with the MO_x layer. This will enhance the sensing response for hydrogen due to large reaction sites available on the activated carbon as well as MO_x at lower operating temperature. Zhang *et al.* [Zhang *et al.*,2018] synthesized the ZnO-C nanofibers using electrospinning method and used them to detect H_2S gas. The ZnO-C nanofibers based sensor showed higher H_2S sensing response (2.55) than pure ZnO nanofibers (1.98) for 1 ppm at 250˚C. Mendoza *et al.* [Mendoza *et al.,* 2014] synthesized the SnO_2-CNTs nanocomposite films by hot filament CVD technique, where SnO_2-CNTs gas sensor displayed better sensitivity towards alcohol vapors and hydrogen than pristine SnO_2 or CNTs based sensors. Chu *et al,* [Chu *et al.,* 2015] reported SnO-graphene composites using hydrothermal method. It was seen that the SnO-1% graphene composites showed good sensing response to formaldehyde vapor and detected 0.001×10^{-6} formaldehyde vapor at 133˚C. The highest sensing response was explained by synergistic effect of the small size of SnO and the good electronic properties of graphene. Zhang *et al.* [Zhang *et al.,* 2015] developed the ZnO/multi-wall carbon nanotubes (ZnO/MWCNTs) film on PCB substrate with interdigitated electrode microstructure using layer-by-layer (Lbl) self-assembly method for ethanol detection. ZnO/MWCNTs sensor depicted highest ethanol sensing response than ZnO and ZnO/PSS for 50 ppm at room temperature. Punginsang *et al.* [Punginsang *et al.,* 2017] fabricated Co-doped SnO_2 nanoparticles with electrolytically exfoliated graphene for ethanol sensing. Excellent sensing response was due to the cumulative effect of catalytic substitutional p-type Co dopants, formation of M-S junctions of graphene-Co- doped SnO_2, and high surface area of micropores in the composites.

In this chapter, polymer blend of homopolymer polyacrylonitrile (PAN) and a block co-polymer (poly(acrylonitrile-block-methylmethacrylate) (PAN-b-PMMA) is used, which is fabricated by electrospinning followed by pyrolysis to yield nanoporous CNF. Therefore, the utilization of CNF is to decorate ZnO nanostructures as gas sensing platform. PAN homopolymer is used to boost the carbon yield, while PAN-b-PMMA contributes to the porosity by the decomposition of PMMA phase in the block copolymer. Sensors based on CNF/ZnO nanostructures demonstrate excellent hydrogen sensing response than pure CNF or pure ZnO nanostructures at moderate temperature. The possible gas sensing is also discussed in the end of this chapter.

6.2 EXPERIMENTAL SETUP

CNF has been synthesized using electrospinning technique. The solution used for electrospinning is prepared by blending of 12 wt.% PAN solution in DMF with 8 wt.% PAN-b-PMMA solution in DMF in ratio 1:1 (v/v). As-spun nanofibers are then thermally annealed at 180˚C in vacuum (-500mm Hg) for 12 h followed by UV exposure for 1 min. After that, degraded PMMA phase is etched out using acetic acid followed by washing with the DI water. Before pyrolysis, the treated nanofibers are stabilized by heating at 250˚C for 1 h in the air. Later on, pyrolysis process has been carried out in a two-stage process in presence of nitrogen atmosphere. First, heating has been done from room temperature to 350˚C with the ramp rate of 3˚C/min and dwelling for 30 min. In the next stage, heating rate is increased to 5˚C/min to reach a final temperature of 900˚C with dwelling time of 1 hour. ZnO nanostructures have been deposited on p-Si substrate by RF magnetron sputtering system. The growth parameters of ZnO nanostructures have been discussed in previous chapter. Then, IDE pattern of Au is deposited on ZnO nanostructures using a thermal evaporator system. In order to give excellent adhesion of Au pattern IDE structures on ZnO nanostructures, the sample has been thermally annealed to 350˚C for 3 hours. Initially, 10 mg CNF flakes are mixed in 10 ml IPA solution, and then the solution is sonicated for 30 minutes to prepare the homogenous solution of dispersed CNF. After that, different concentrations of CNF are loaded on Au-IDE pattern ZnO nanostructures by drop cast method. In this approach, 10µL of the homogenous solution of a different concentration of CNF (0.1 – 0.5 wt%) is loaded onto IDE pattern. After that, the samples are annealed in furnace for 15 minutes at 100˚C for complete removal of solvent. The schematic diagram of CNF/ZnO nanostructures based sensor is shown in Figure 6.1.

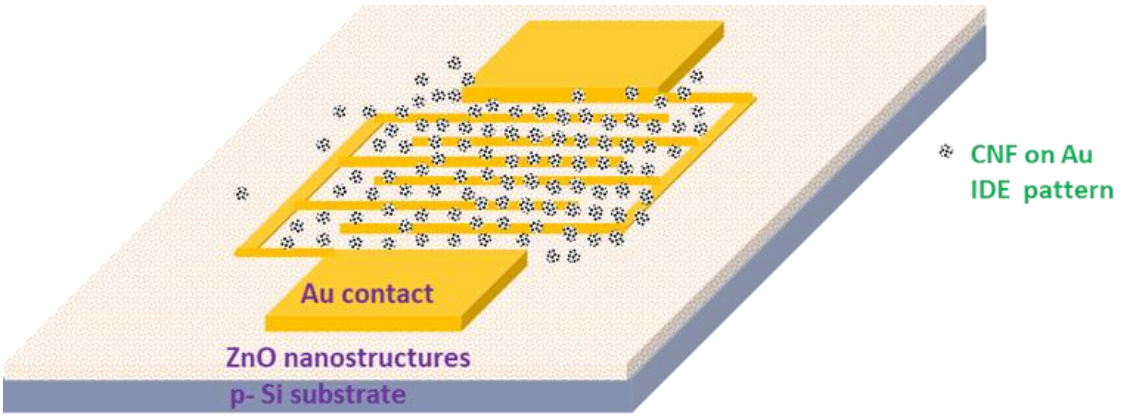

Figure 6.1: Schematic diagram of CNF/ZnO nanostructures based device

Optical images of pure CNF and different concentrations of CNF (0.1 – 0.5 wt%)/ZnO nanostructures are shown in Figure 6.2 (a-f).

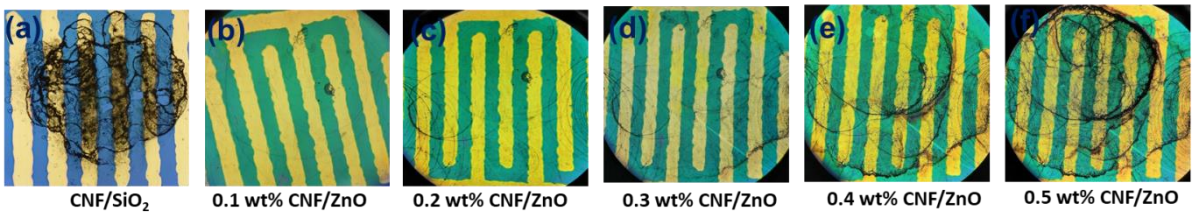

Figure 6.2: Optical image of (a) pure CNF and (b-f) different concentration of CNF (0.1-0.5 wt%)/ZnO nanostructures

Initially, CNF is dispersed on IDE/SiO_2 sample as seen in Figure 6.2 (a). It is noticed that the CNF has been formed as a network structure on the IDE/SiO_2. When the concentration of CNF changes from 0.1 to 0.5 wt%, the formation of network like structures between the IDE also increases as seen in Figure 6.2 (b-f).

6.3 STRUCTURAL ANALYSIS

XRD characterization of different concentrations of CNF, ZnO, and CNF (0.1-0.5 wt%) loaded on ZnO nanostructures has been performed. Figure 6.3 (a) shows XRD spectra of CNF where the major peak (0 0 2) is centred at 24.8˚ and the minor peak (1 0 0) is centred at 43.5˚.

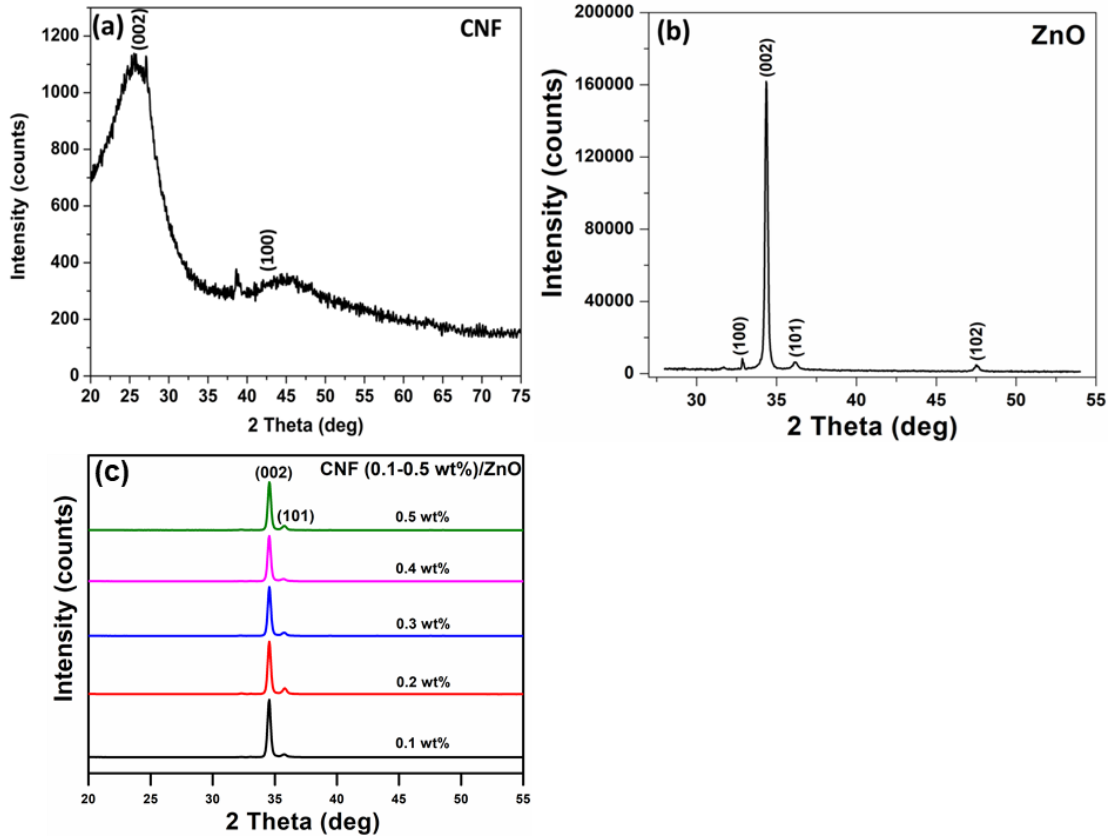

Figure 6.3: XRD pattern of (a) CNF (b) ZnO nanostructures (c) different concentrations of CNF (0.1–0.5 wt%) loaded on ZnO nanostructures

The presence of broad Bragg peaks also suggests the presence of nanographitic structures [Cho *et al.*, 2014]. The interlayer spacing is found to be 0.358 nm using the Bragg's equation; whereas XRD pattern of ZnO nanostructures represent the main peak (002) along c- axis in Figure 6.3 (b). This peak suggests that ZnO is highly crystalline having wurtzite structure. Figure 6.3 (c) depicts the XRD characterization of CNF (0.1-0.5 wt%)/ZnO nanostructures. In all samples, it can be seen that ZnO represents strong peak at (002) plane which confirms the hexagonal

wurtzite structures along c- axis. However, a small peak at (101) is also perceived. These results notify highly crystalline nature of ZnO. Moreover, there are no peaks detected for different concentrations of CNF. These phenomena might be due to small concentration of CNF present on ZnO surface. The same behavior can be observed in rGO/ZnO nanostructures [Anasthasiya *et al.,* 2018; Drmosh *et al.,* 2019]. Peak at 1360 cm^{-1} (D - band) in the Raman spectra of CNF is associated with the disordered structures and crystal defects in carbon materials, while the peak at 1587 cm^{-1} (G - band) is associated with the phonon mode with E_{2g} symmetry of graphite shown in Figure 6.4 [Yan *et al.,* 2015].

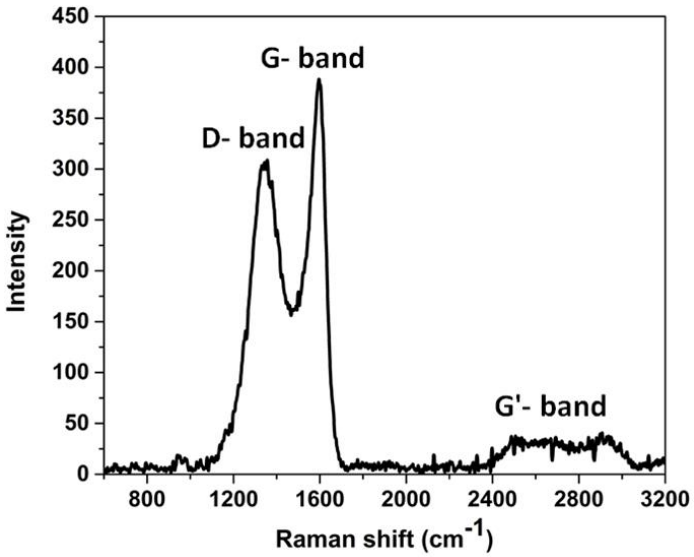

Figure 6.4: Raman Spectra of CNF

Also, the broad peak centred at 2750 cm^{-1} (G' - band) is the characteristic of undisturbed graphitic lattices, which indicates formation of amorphous carbons with nanographitic structures [Byun *et al.,* 2011, Yan *et al.,* 2015]. The intensity ratio (I_d/I_g) is found to be 0.79 and the in-planar crystallite thickness is calculated as 5.57nm ($R= 4.4/(I_d/I_g)$).

6.4 SURFACE MORPHOLOGY ANALYSIS

The morphological analysis of CNF, ZnO, and CNF (0.1-0.5 wt%)/ZnO nanostructures can be seen from FESEM images as shown in Figure 6.5 (a-h). It can be observed that CNF has three dimensional interlinked network structures in Figure 6.5 (a). Average fiber diameter of CNF is measured to be 87.1 ± 11.4 nm. Figure 6.5 (b) shows highly dense ZnO nanostructures which are uniformly grown throughout the p-Si substrate. It is clearly seen that the CNF is well decorated on ZnO nanostructures in Figure 6.5 (c). It is obvious that the amount of decorated CNF between the two electrodes increases with increase in the amount of CNF on ZnO by drop casting.

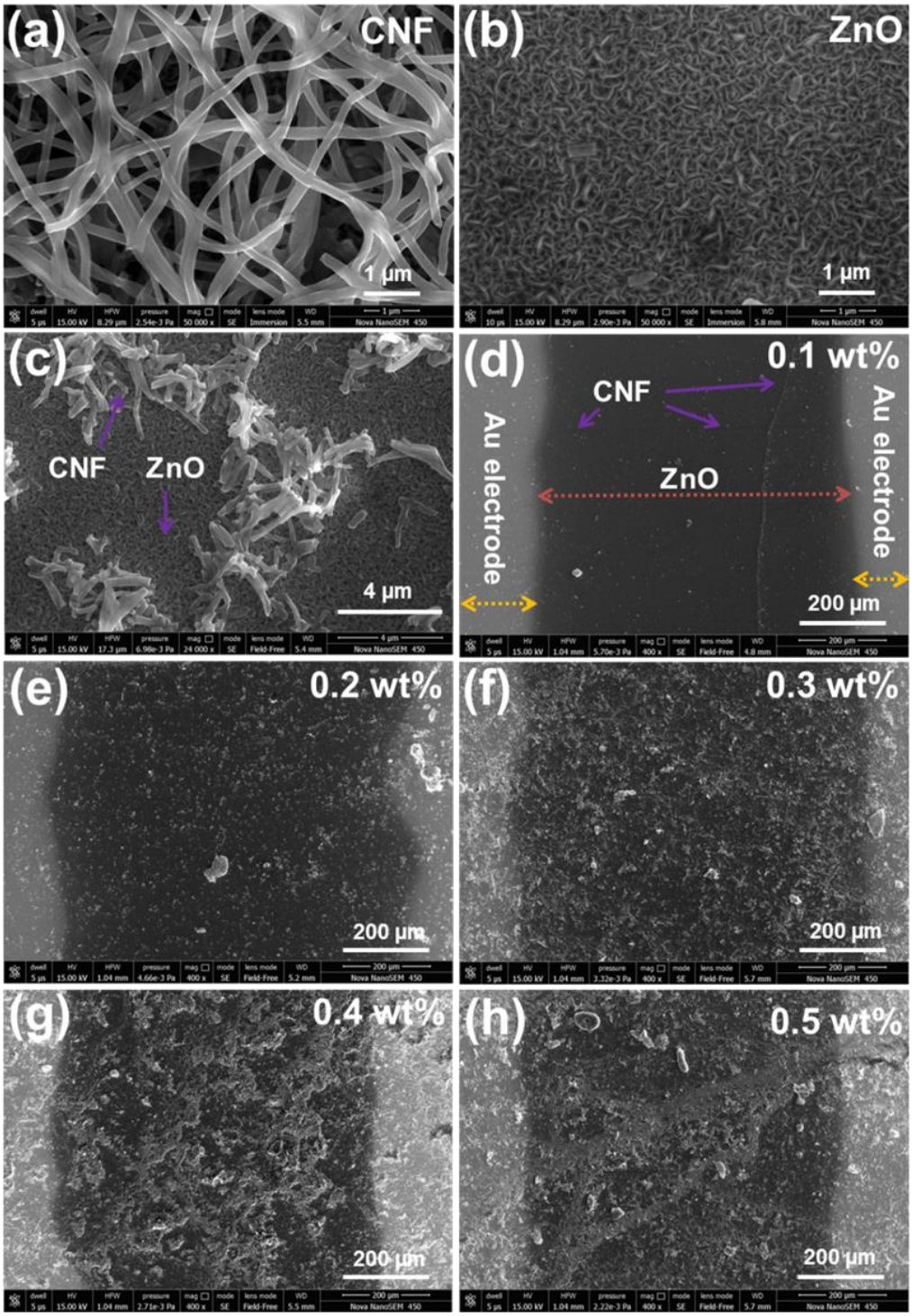

Figure 6.5: FESEM images of (a) CNF (b) ZnO (c) CNF decorated on ZnO (d) 0.1 wt% CNF/ZnO (e) 0.2 wt% CNF/ZnO (f) 0.3 wt% CNF/ZnO (g) 0.4 wt% CNF/ZnO (h) 0.5 wt% CNF/ZnO

Figure 6.5 (d) shows 0.1 wt% CNF decorated between two electrodes. Initially, there are less number of CNF particles present on ZnO nanostructures, which formed limited number of p-n heterojunctions between the electrodes. After that, the amount of p-n heterojunction is increased for 0.2 wt% CNF loading on ZnO nanostructures. At this concentration, the amount of p-n heterojunction becomes highest, and CNF does not fully cover the ZnO surface. At high concentration (0.3-0.5 wt% CNF), the amount of CNF increases drastically. Figure 6.5 (h) shows partial bridge like network of CNF (0.5 wt%) between the two electrodes and ZnO nanostructures that are also covered by CNF.

6.5 FTIR ANALYSIS

Figure 6.6 (a) represents the FTIR spectrum of PAN/PAN-b-PMMA as-spun and as derived carbon nanofibers. For as-spun nanofibers, the bands observed at 2940 cm^{-1} and 2995 cm^{-1} are attributed to the C-H stretching vibration of the aromatic functional group, and the corresponding bending vibration is obtained at 1448 cm^{-1} [Zhou *et al.*, 2008].

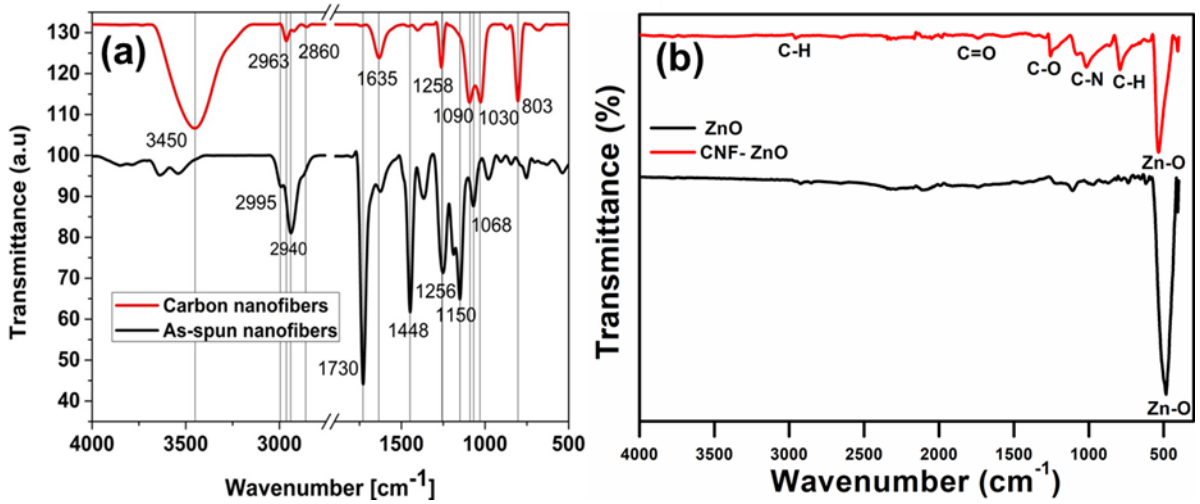

Figure 6.6: FTIR spectra of (a) CNF (b) pristine ZnO and CNF loaded on ZnO nanostructures

The peak obtained at 1730 cm^{-1} is the characteristic adsorption peak of PMMA block due to C=O bond. The peaks at 1068 cm^{-1}, 1150 cm^{-1}, and 1256 cm^{-1} are due to the stretching vibrations of sp^3 hybridized and sp^2 hybridized C-O bonds in PMMA block, respectively. For the carbon nanofibers, the band at 3450 cm^{-1} is attributed to hydroxyl group, whereas the peaks at 2963 to 2860 cm^{-1} are mainly due to methylene bridge. The peak at 1635 cm^{-1} is assigned to the vibration of benzene ring skeleton [Ma *et al.*, 2014], and that at 1090 cm^{-1} and 1030 cm^{-1} is coming from the C-N stretching vibration. Further, the peaks at 803 cm^{-1} and 1258 cm^{-1} are due to C-H bending and C-O stretching vibrations, respectively [Araga *et al.*, 2017]. Figure 6.6 (b) shows FTIR spectra of ZnO and CNF loaded ZnO nanostructures. In case of ZnO, highly intense absorption peak is observed at 495 cm^{-1}, that occurs mainly due to the stretching vibration of Zn-O bond [Zhang *et al.*, 2018]. However, the peak intensity of stretching vibration for Zn-O bond in CNF loaded ZnO nanostructures is decreased because of the presence of CNF on ZnO surface. In addition, other oxygen functional groups are also present which are highly essential for enhancing the sensing performance of the sensor.

6.6 ELECTRICAL MEASUREMENT

I-V characterization of all samples have been measured at room temperature, and then compared with different concentrations of CNF (0.1-0.5 wt%)/ZnO nanostructures as shown in Figure 6.7.

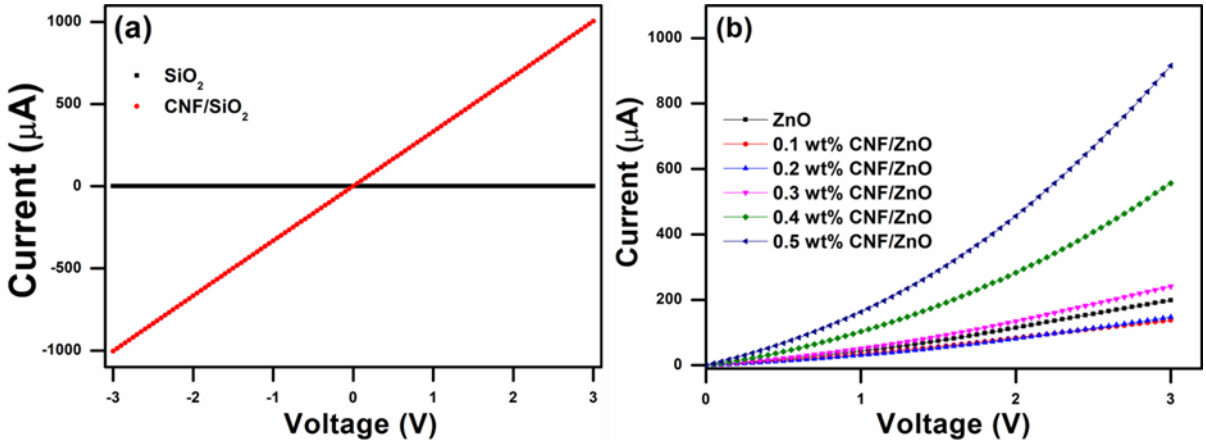

Figure 6.7: Room temperature I–V characteristics of (a) CNF/SiO_2 versus SiO_2 (b) ZnO versus (0.1-0.5 wt%) CNF/ZnO

It is noticed that the trend of current conduction strongly depends upon the loading amount of CNF over ZnO nanostructures. Firstly, CNF/SiO_2 film exhibits ~1mA current as compared to SiO_2 substrate at 3V as shown in Figure 6.7 (a). The occurrence of large current is mainly caused by an excellent conductivity of CNF film, wherein the electrons follow the shortest path between the electrodes and conduction takes place through connecting CNF networks. Most interestingly, the sensor based on CNF/ZnO shows a decrease in current as compared to pure ZnO nanostructures from 198 to 147 μA when the concentration of CNF is increased up to 0.2 wt% at 3V forward bias, as can be seen in Figure 6.7 (b). This decrease in current may be due to the formation of p – n heterojunction between CNF and ZnO nanostructures because the CNF shows p – type behaviour, which leads to an increased resistance of the sensor [Liao *et al.*, 2009; Wang *et al.*, 2015]. The current however, is found to increase when the concentration of CNF increases up to 0.5 wt%. The increased current in CNF/ZnO nanostructures predominately is due to network formation of CNF between the IDEs. Moreover, the electrons follow this route for conduction through p – n heterojunction between CNF and ZnO nanostructures, which can be clearly observed with high concentration of CNF (0.3 – 0.5 wt%) as shown in Figure 6.5 (f-h) as well as in Figure 6.7 (b). Thus, resistance has been decreased for higher concentration of CNF (0.3-0.5 wt%) in CNF/ZnO nanostructures based sensors.

6.7 GAS SENSING MEASUREMENT

Hydrogen gas sensing response of CNF, ZnO nanostructures, and different concentration of CNF (0.1 – 0.5 wt%)/ZnO nanostructures are detected for 100 ppm at 150˚C. It is thus observed that MO_x based gas sensors usually depend upon the target gas concentration and operating temperature. Figure 6.8 (a) shows the dynamic sensing response of CNF, ZnO nanostructures, and CNF/ZnO nanostructures with varied concentrations of CNF (0.1 – 0.5 wt%) towards 100 ppm hydrogen at 150˚C.

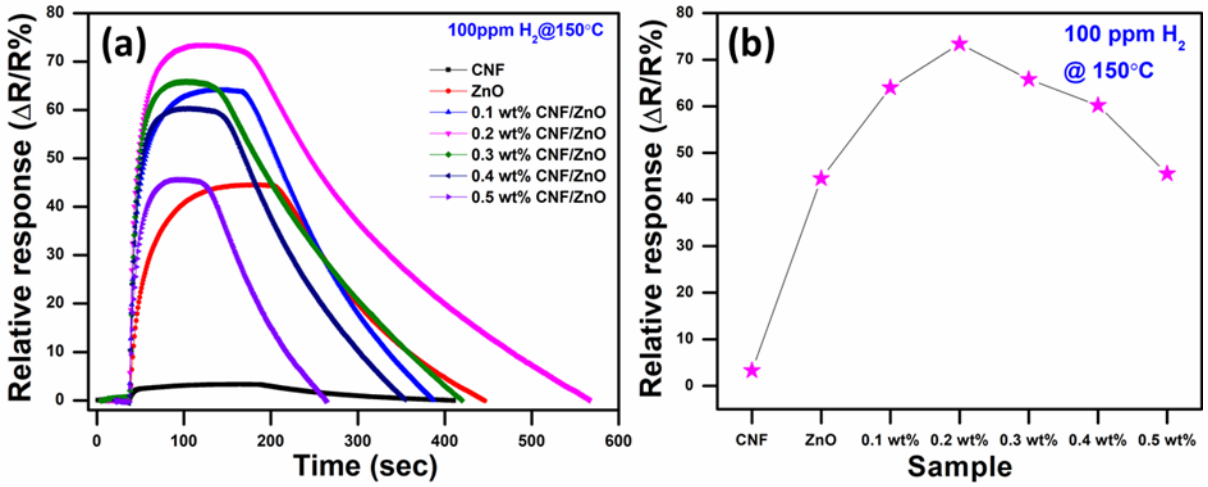

Figure 6.8: Comparison of relative response; (a) Dynamic sensing response (b) Maximum relative response for all sensors for 100 ppm hydrogen gas at 150 °C

It can be observed that the relative response of CNF and ZnO nanostructures is around 3.29% and 44.51%, respectively. Moreover, the relative response of CNF/ZnO nanostructures is found to increase when the CNF concentration rises to 0.2 wt%. For such concentration of CNF, maximum relative response of ~73.4% occurred in the same condition. However, loading CNF at higher concentration (0.3 – 0.5 wt%) on ZnO nanostructures reduces the relative response upto 45.55% for 0.5 wt% CNF/ZnO nanostructures. Hence, the maximum relative response is achieved by 0.2 wt% CNF/ZnO nanostructures than pure CNF and pure ZnO nanostructures according to Figure 6.9.

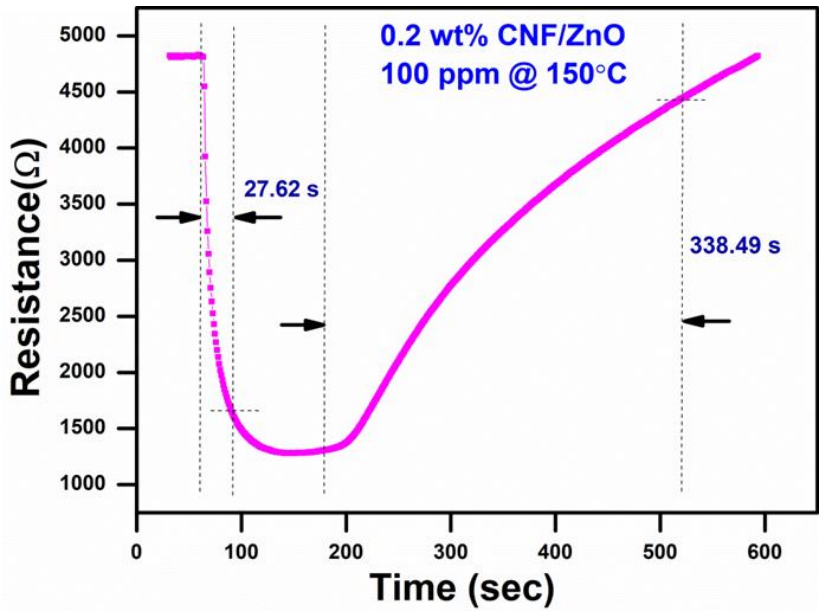

Figure 6.9: Response time and recovery time for 0.2 wt% CNF loaded ZnO nanostructures

The response and recovery time of 0.2 wt% CNF/ZnO nanostructures are calculated as 27.62 s and 338.49 s, respectively. Sensor based on 0.2 wt% CNF/ZnO nanostructures is operated at 1.86 mW, which makes it satisfy the predominant condition of low operating power to qualify as an excellent gas sensor. Relative response of 0.2 wt% CNF/ZnO nanostructures for hydrogen gas in different concentrations from 1 to 100 ppm at 100˚C is shown in Figure 6.10.

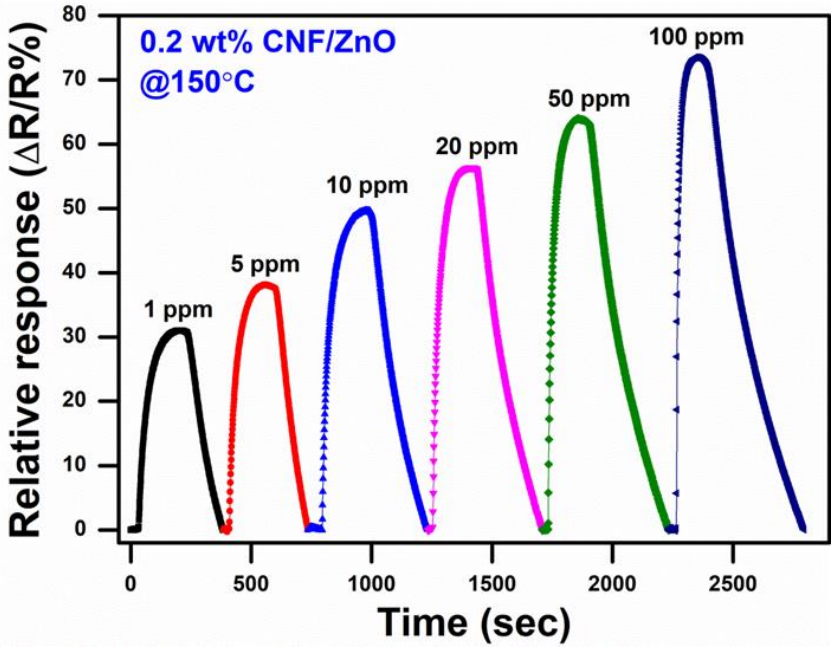

Figure 6.10: Relative response curve for 0.2 wt% CNF/ZnO nanostructures from 1 to 100 ppm hydrogen gas at 150 ℃

These results suggest that the response enhances with increasing concentration of hydrogen gas. Moreover, the repeatability of 0.2 wt% CNF/ZnO nanostructures based sensor is evaluated for three cycles continuously for 100 ppm concentration at 100˚C, as represented in Figure 6.11.

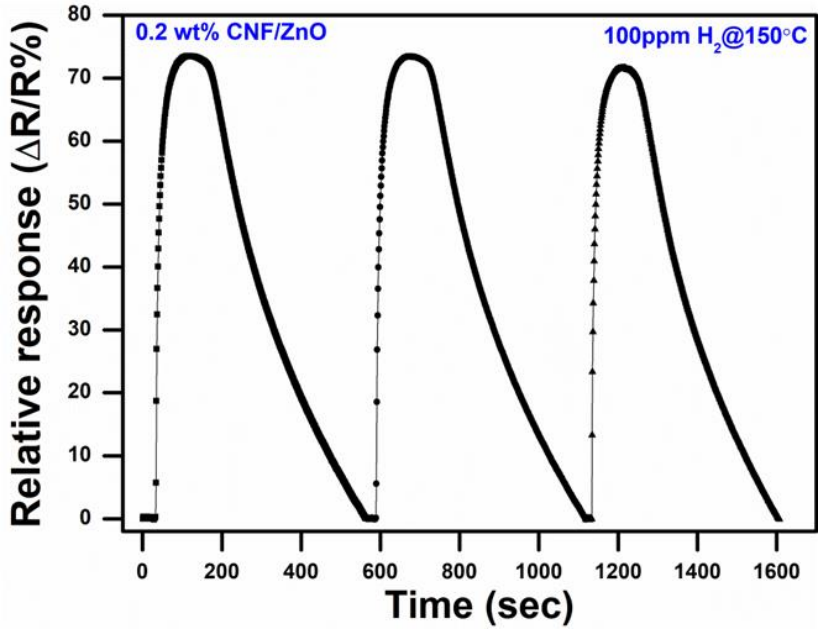

Figure 6.11: Repeatability curve of 0.2 wt% CNF/ZnO nanostructures based sensor for hydrogen gas at 100 ppm at 150 ℃

The behavior of all three sensing response cycles reveals good repeatability under the same condition. Table 6.1 shows the comparative investigation of hydrogen gas sensor demonstrated in present work with other hydrogen sensors reported in past literature.

Table 6.1: Comparison of hydrogen gas sensing performance of different ZnO based sensors

S.N	*Sensing material*	*H_2 (ppm)*	*Response*	*Response time (sec)*	*Recovery time (sec)*	*Temp. (°C)*	*Reference*
1.	Pt/Pd bimetallic core-shell nanoparticles decorated ZnO nanorods	10000	58% (ΔR/R)	5	76	100	Hassan *et al.*, 2017
2.	ZnO nanowires	50	2.62 (R_a/R_g)	-	-	300	Drobek *et al.*, 2016
3.	Cd doped ZnO nanorods	500	2.6 (R_N/R_H)	63	-	150	Yang *et al.*, 2015
4.	Pd decorated SnO_2 nanowires	100	27.84 (R_a/R_g)	-	-	300	Kim *et al.*, 2019
5.	WO_3 nanoparticles decorated ZnO nanowires	2000	12.6 (R_a/R_g)	-	-	200	Park *et al.*, 2019
6.	NiO/rGO nanocomposite	10000	0.64 (ΔR/R)	28	142	50	Ren *et al.*, 2018
7.	ZnO/SIM-1 composite nanowires	50	2.56 (R_a/R_g)	-	-	300	Drobek *et al.*, 2018
8.	Er doped SnO_2 nanostructures	100	28 (R_a/R_g)	11	42	360	Singh *et al.*, 2019
9.	CNF loaded ZnO nanostructures	100	73.54% (ΔR/R)	29.66	326.22	150	This work

Among all above mentioned sensors, the hydrogen gas sensor based on CNF loaded ZnO nanostructures shows excellent sensing properties as compared to other sensors.

6.8 GAS SENSING MECHANISM

Sensing results show that a favorable amount of CNF (~ 0.2 wt%) boosts the relative response for hydrogen gas than pure CNF and pure ZnO nanostructures. The perceived hydrogen sensing performance can reasonably be explained by the formation of p–n heterojunction where the CNF shows p–type behavior. This leads to increased adsorption and reaction of hydrogen gas at the interface between CNF and ZnO nanostructures, which can also be described by the energy band diagram as well as schematic diagram shown in Figure 6.12 (a-e). When both CNF and ZnO are not in contact, the Fermi level of CNF is lower than ZnO due to higher work function of CNF (4.6 eV) than ZnO (4.3 eV) ($\phi_{ACs} > \phi_{ZnO}$) [Zhang *et al.*, 2011; Xia *et al.*, 2016]. However, the position of Fermi levels becomes equal when both materials combine

with each other. This is attributed to the movement of electrons from ZnO to CNF resulting in the formation of p–n heterojunction between them. Thereafter, the electrons will be extracted from the ZnO surface in presence of air because the electronegativity of oxygen molecules is higher than that of ZnO. Consequently, these oxygen molecules will change into oxygen ions on the ZnO surface, thus creating an electron depletion layer on the ZnO surface as shown in the Eqs. (6.1) and (6.2). Furthermore, the depletion width as well as barrier height increase at the interface between CNF and ZnO nanostructures with increased sensor's resistance than pure ZnO nanostructures. The increased barrier height and depletion width are mainly due to several types of oxygen species such as, oxygen functional groups, as shown in FTIR analysis. Initially, the CNF is distributed individually between the electrodes throughout the ZnO nanostructures at low amounts of CNF (0.1 - 0.2 wt%), which is clearly visible in FESEM images as shown in Figure 6.5 (d-e). This leads to creation of large number of p – n heterojunctions at the interface between CNF/ZnO nanostructures, and significant increase in the depletion width as well as barrier height, resulting in reduced current as compared to pure ZnO nanostructures.

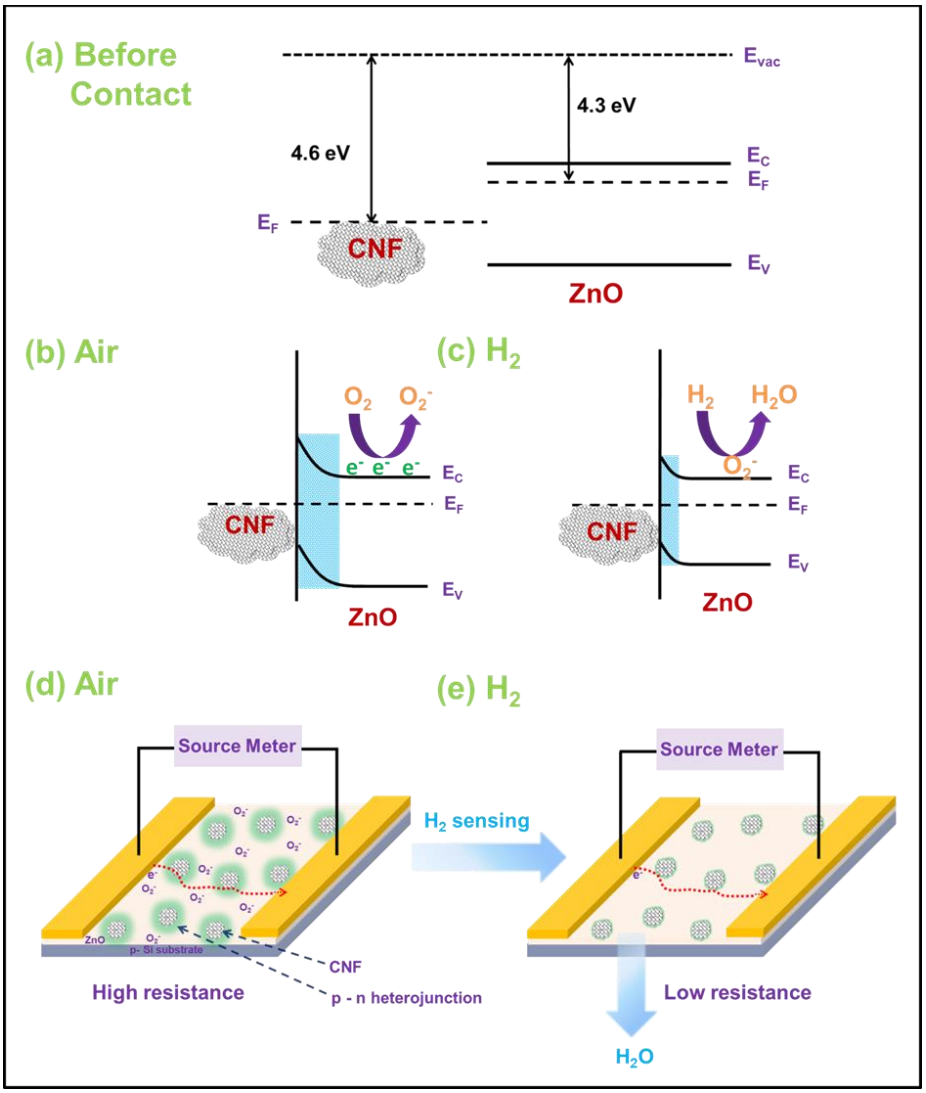

Figure 6.12: Band diagram demonstration of CNF/ZnO nanostructures (a) before contact and (b–c) after contact (presence of air and hydrogen) and (d–e) schematic diagram for hydrogen sensing mechanism

These results are also evident from the *I-V* characteristics of all samples. When the sensor is exposed to hydrogen gas, the oxygen species will react with the hydrogen molecules according to the Eq. (6.3).

$$O_{2(gas)} \rightarrow O_{2(ads\ on\ ZnO)} \quad (6.1)$$

$$O_{2(ads\ on\ ZnO)} + e^-_{(from\ ZnO\ surface)} \rightarrow O^-_{2(ads\ on\ ZnO)} \quad (6.2)$$

$$O^-_{2(ads\ on\ ZnO)} + 2H_2 \rightarrow 2H_2O + e^-_{(to\ ZnO\ surface)} \quad (6.3)$$

Therefore, the electrons are liberated from oxygen species, and returned into the conduction band of ZnO, which results in reduction of resistance as well depletion layer. Excluding the basic mechanism of hydrogen sensing for ZnO nanostructures, the relative response of 0.2 wt% CNF/ZnO is more than pure CNF and pure ZnO which may be explained by the following points. Firstly, the CNF consists of a large number of nanoporous structures with high surface area, which helps the hydrogen molecules to easily diffuse through nanoporous CNF, and later reach the ZnO nanostructures. Such type of movements of hydrogen molecules not only react with the high surface area of CNF, but also reacts with the active sensing layer (ZnO nanostructures), resulting in higher relative response due to the availability of a large number of oxygen sites. Secondly, the availability of a massive quantity of p – n heterojunction creates more depletion width plus barrier height, which also enhances the number of oxygen ions. Furthermore, drastic reduction in depletion width as well as barrier height takes place in presence of hydrogen gas. Consequently, one can observe enhanced relative response with 0.2 wt% CNF/ZnO sensor than the response with pure form of CNF and ZnO.

Additionally, the existences of hydrophobic oxygen functional groups on CNF surface will also assist in providing active sites for incoming hydrogen molecules, and in turn improving the sensing response. However, higher amount of CNF (0.3 – 0.5 wt%) loading starts forming partial bridges of CNF network like structures between the electrodes. Under this condition, the oxygen species and p–n heterojunction on the CNF/ZnO will be less effective because the electrons follow the path of partial bridges of CNF network during conduction between the electrodes. Thus, current through high amount of CNF/ZnO nanostructures will be higher than the optimum amount (0.2 wt%) of CNF/ZnO nanostructures, which can also be seen in *I-V* characteristics. Hence, a reaction with hydrogen gas results in decreased relative response as compared to 0.2 wt % CNF/ZnO. This is due to the fast movement of electrons between the electrodes as the p – n heterojunction and oxygen species are less affected. Moreover, the occurrence of a higher amount of CNF network on ZnO surface also reduces the active sensing area, hence restricting the interaction of hydrogen gas for reaction, further degrading the sensing response.

6.9 CONCLUSION

To summarize this chapter, hydrogen sensing has been performed on PAN/PAN-b-PMMA derived electrospun nanoporous CNF loaded on ZnO nanostructures. Different concentrations of CNF (0.1 – 0.5 wt%) are loaded on sputter grown ZnO nanostructures by drop cast method. FESEM images of all sensors have been extracted systematically after loading different concentrations of CNF on ZnO surface. XRD characterization reveals that CNF and ZnO have good crystalline nature. Initially, loading of small amount of CNF (0.1 – 0.2 wt%) leads to decreased current as compared to pure ZnO nanostructures, but the current increases significantly for high amount of CNF (0.3 – 0.5 wt%). Maximum relative response is observed for 0.2 wt% CNF/ZnO nanostructures than all sensors towards 100 ppm hydrogen at 150˚C. In fact, improved sensing response is mainly due to large reaction sites available for hydrogen molecules while diffusing through the nanoporous CNF, the creation of numerous p – n heterojunctions at the interface of CNF and ZnO, and the occurrence of additional oxygen functional groups at the CNF surface. Moreover, the sensing response decreases for high amount of CNF loading on ZnO nanostructures, which is due to the fact that current passes directly through the partial bridges of CNF network between the electrodes making p – n heterojunctions less effective. Therefore, one can conclude that these results can be utilized to

develop reliable and robust hydrogen gas sensors at elevated temperature with high sensitivity, and quick response, for domestic as well as industrial applications.